
CHAPTER 5: ELECTROCHEMICAL TURBULENCE

In chapter 2 the $\text{Pt}|\text{H}_2\text{SO}_4, \text{Cl}^-, \text{Cu}^{2+}|\text{H}_2$ system was introduced as a prototype electrochemical oscillator which exhibits a large variety of different current oscillations under potentiostatic control as well as potential oscillations when subjected to galvanostatic control. This chapter inaugurates the systematic investigation on the spatiotemporal pattern formation in the $\text{Pt}|\text{H}_2\text{SO}_4, \text{Cl}^-, \text{Cu}^{2+}|\text{H}_2$ system under potentiostatic control. For the occurrence of spatial patterns the way in which different positions of the medium, that is the electrode surface in the present case, are coupled among each other plays a pivotal role. In this sense, it was stressed in chapter 2 that there are basically two types of spatial couplings in electrochemistry

systems: migration coupling and global coupling. An important peculiarity of migration coupling is the fact that its range can be varied. This chapter focuses on the migration coupling, and the influence of its range on pattern formation is investigated.

5.1 INTRODUCTION

Krischer and coworkers [26, 47] reported the first spatially resolved experiments on the oscillatory $\text{Pt}|\text{H}_2\text{SO}_4, \text{Cl}^-, \text{Cu}^{2+}|\text{H}_2$ system. In ref. [47] the authors investigated the system's spatiotemporal dynamics when subjected only to the migration coupling as well as in the additional presence of the negative global coupling (NGC). Figure 5.1 exemplifies the spatiotemporal evolution of the inhomogeneous part of the interfacial potential, $U_{\text{PP}} - \langle U_{\text{PP}} \rangle_x$, together with the corresponding current time series in the absence of the NGC. As clearly seen, the homogenous interfacial potential distribution (i.e., the $U_{\text{PP}} - \langle U_{\text{PP}} \rangle_x$ values around zero and colored in green) is broken up only when the current abruptly changes its state from passive (low) to active (high) and vice versa. These *spatially modulated oscillations* were found in the entire voltage window in the oscillatory region and result of a spatial instability of the homogeneous limit cycle.

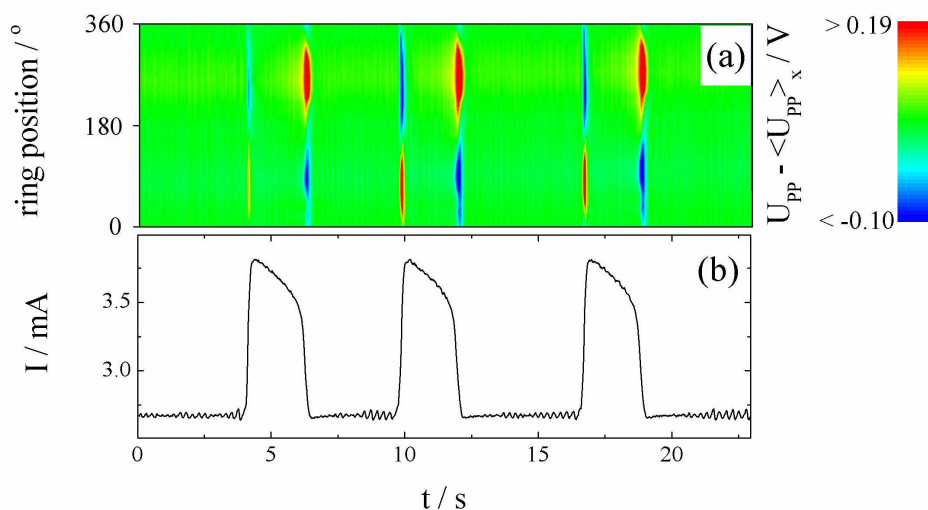


Figure 5.1: (a) Spatiotemporal picture of the inhomogeneous part of the interfacial potential as a function of the ring position and time, and (b) potentiostatic current time series. In this experiment the electrolyte consisted of 0.5 mM H_2SO_4 , 0.1 mM HCl , and 0.025 mM CuSO_4 , saturated with H_2 . Rotation rate of the WE $\omega = 20$ Hz, an external RE was used and $U = 2.05$ V vs. RHE. After Grauel *et al.* [47].

In this work, the authors have speculated that the system displaying these modulated oscillations would be classified as a Benjamin-Feir (BF) unstable system, following an argumentation first given by Christoph [46, 78]. The BF instability implies that uniform oscillations are unstable with respect to small spatial perturbations [51]. In BF unstable systems one would, in fact, expect the occurrence of spatiotemporal chaos or chemical turbulence [48]. However, in this system [47] the characteristic length of the observed pattern was of the same order of magnitude as the length of the system, and instead of a turbulent regime only regular limit cycle oscillations were observed.

Further investigations of this system were carried out in the framework of this thesis and are reported in this chapter. Compared to the cited experiments (see Figure 5.1) [47], a 2.5 times lower copper concentration was used here. In section 5.2 the experimental strategy adopted as well as the system's voltammetric response are presented. Results on the impact of the separation between counter and reference electrodes on the dynamics behavior are described in sections 5.3 and 5.4. In section 5.5 the observed patterns are characterized via Karhunen-Loève Decomposition (KLD). The main findings are discussed and summarized in section 5.6.

5.2 EXPERIMENTAL STRATEGY

The potentiostatic experiments were carried out in two different configurations in order to study the effect of the localization of the migration coupling (s.b.) (Figure 5.2). In both cases the external RE (i.e., in a position equivalent to a point below the CE plane, see chapter 3) was used. The separation between the CE and the WE was varied, and two cases were investigated. In the first case the 'conventional' setup, in which the CE/WE distance was 40 mm, was adopted, in the second situation the adjustable CE was brought to the WE up to a separation of 5 mm. Figure 5.3 schematically shows these two situations that are referred to hereafter as cases 1 and 2.

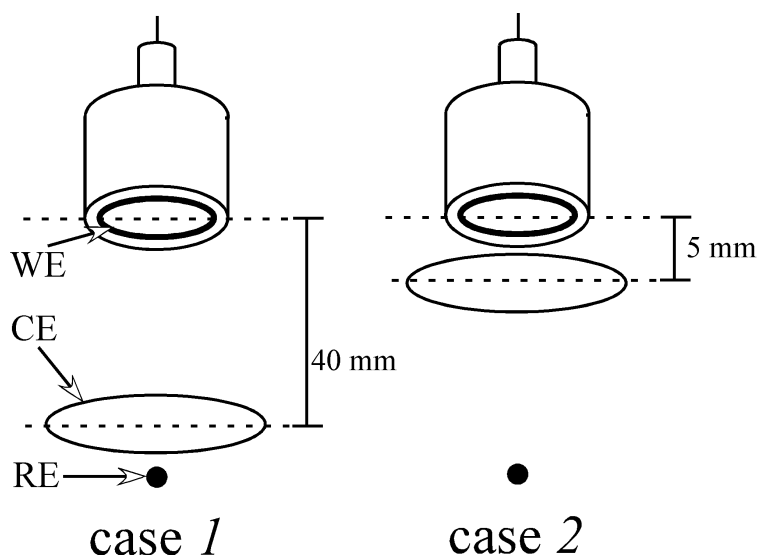


Figure 5.2: Experimental setup showing the two different electrode arrangements: in case 1 the distance between the CE and the WE is 40 mm and in case 2 the CE/WE separation is 5 mm. In both cases the external RE (for details see chapter 3) was used.

In Figure 5.3 the forward voltammetric sweeps corresponding to these two different cases are depicted. In plate (a) the I/U responses were recorded at 0.05 Vs^{-1} and in (b) at 0.01 Vs^{-1} .

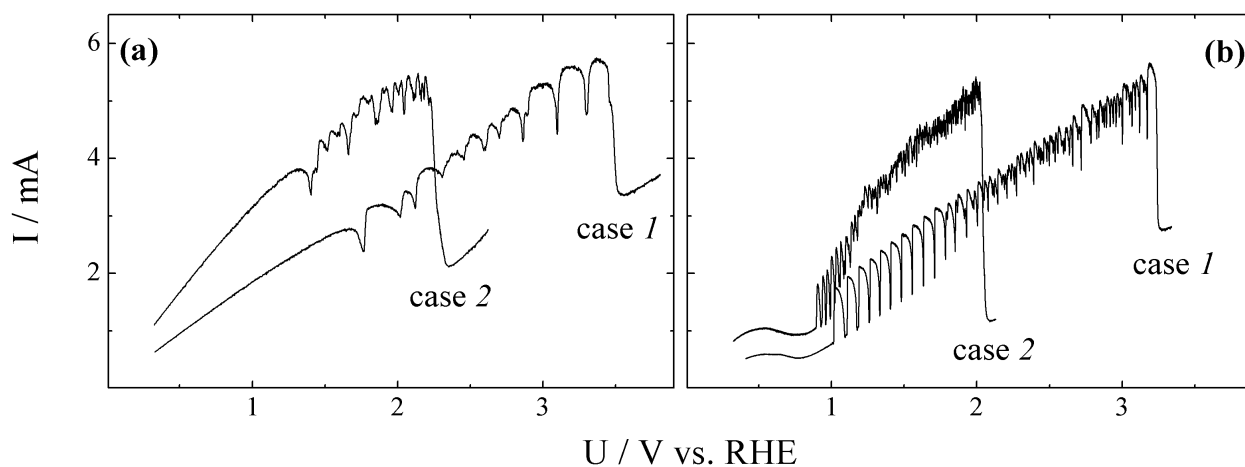


Figure 5.3: I/U curves at (a) 0.05 Vs^{-1} and (b) 0.01 Vs^{-1} for cases 1 and 2 (see Figure 5.2). R_{Ω} ($= R_u$) = $510 \pm 10 \Omega$ and $320 \pm 10 \Omega$ for cases 1 and 2, respectively. The electrolyte consisted of 0.5 mM H_2SO_4 , 0.1 mM HCl , and 0.01 mM CuSO_4 , saturated with H_2 . Rotation rate of the WE $\omega = 20 \text{ Hz}$.

The striking difference between the I/U responses of cases 1 and 2 is caused by the different values of the uncompensated resistances, R_u (which in this case is identical to the cell resistance R_Ω) and can be anticipated from the I/U slopes at the different CE/WE separations. The slower scan (0.01 Vs^{-1}) profiles shown in Figure 5.3 (b) evidence that from an applied voltage on the oscillation frequency increases and the global oscillations become more irregular for both configurations. In the next section, spatially resolved stationary experiments at different values of fixed U are described.

5.3 CASE 1: CE/WE DISTANCE OF 40 mm

Figure 5.4 depicts global current oscillations and corresponding space-time plots of the inhomogeneous part of the interfacial potential obtained at different applied voltages. The first experiment shown in (a) and (b) was obtained at the lowest applied potential, $U = 1.06 \text{ V}$. It is qualitatively similar to the one depicted in Figure 5.1. The large amplitude, relaxation-like current oscillations (Figure 5.4 (a)) are characterized by fast passive/active, i.e., low/high, current transition. Differently from the results depicted in Figure 5.1, the system does not spend much time at the low current state. The spatiotemporal evolution of $U_{PP} - \langle U_{PP} \rangle_x$ displayed in plate (b) shows a spatial symmetry breaking accompanying the fast current transitions. These modulated oscillations (MOs) accompanying the steep current transitions were always found in the entire voltage window in the oscillatory region in the absence of NGC, when a higher copper concentration was used (see ref. [47] and further discussion in chapter 7). Just as in Figure 5.1 [47] the spatial structures popping up during the fast changes of the current can be described as an oscillating sinusoidal structure of wave number 1 whereby the sign of the amplitude is different for increasing and decreasing currents. In the case shown in Figure 5.4 (b), however, this structure is strongly excited in the passive/active transition, and it is hardly seen in the active/passive transition.

Increasing the applied voltage (cf. Figures 5.4 (c) and (d)) the time series becomes less regular whereby first a period-2 state seems to develop, i.e., every second oscillation looks alike. The apparent period-2 manifests itself also in the spatiotemporal behavior. Differently from the above discussed case (Figure 5.4 (b)), an inhomogeneous structure does not only develop on the fast flanks of the current but exists now in a large interval during which the current slowly decreases. Here it is most remarkable that the sign of the amplitude of this pronounced structure changes every oscillation. For example, at a position around 270° the

inhomogeneous oscillations take on a minimum during the first oscillation of the current and a maximum during the second, reflecting the period-2 character of the global time series.

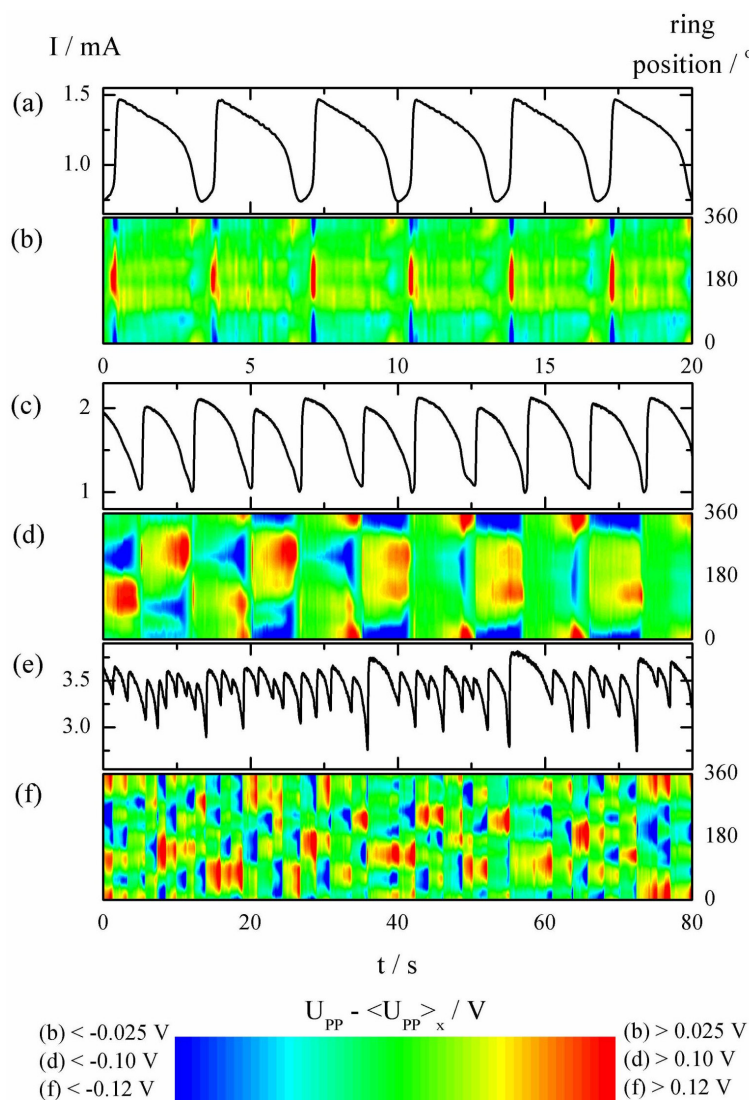


Figure 5.4: (a), (c), and (e): Current time series; and (b), (d), and (f): Spatiotemporal evolution of the inhomogeneous part of the interfacial potential, $U_{PP} - \langle U_{PP} \rangle_x$, as a function of the ring position and time. Applied voltage: (a) and (b) 1.06 V; (c) and (d) 1.19 V; and (e) and (f) 2.14 V. Data obtained with configuration ‘case 1’. The remaining experimental conditions are identical to those in Figure 5.3. The color code is different in the three cases and is given besides the color bar at the bottom.

At higher U values a rather irregular motion replaces the nearly periodic structures observed at lower U . This can be seen in the temporal evolution of the global current shown in Figure 5.4 (e) which was obtained at $U = 2.14$ V. The spatiotemporal pattern degenerates into a turbulent state characterized by the excitation of several regions along the ring in an apparently random manner, as shown in Figure 5.4 (f).

In all spatiotemporal plots depicted in Figure 5.4 the inhomogeneous part of the dynamics was displayed, this means the homogeneous mode has been subtracted from the interfacial potential signal, U_{pp} . Noteworthy in the sequence shown in Figure 5.4 for increasing U , i.e. from (a) to (e), is the fact that the amplitude of the inhomogeneous part of the interfacial potential increases. As further discussed below, an important point for the characterization of the dynamics is the understanding of the role of the homogeneous mode as well as its contribution to the dynamics. Figure 5.5 shows three space-time plots of the data presented in Figures 5.4 (b), (d), and (f), but now in terms of the entire U_{pp} evolution, i.e., including also the homogeneous mode. In Figures 5.5 (b) and (c), a shorter time interval than in Figures 5.4 (d) and (f), is presented for easier visualization.

In the first case, Figure 5.5 (a), the oscillations are nearly homogeneous, and spatial structures become visible only after subtraction of the homogeneous mode, as done in Figure 5.4 (b).

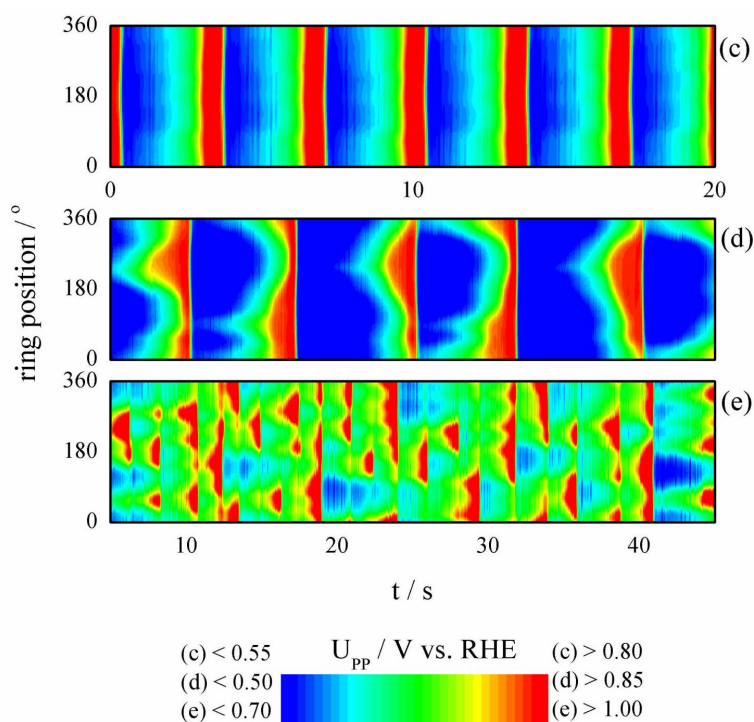


Figure 5.5: Spatiotemporal evolution of the interfacial potential, U_{pp} . Data shown in (a), (b), and (c) belong to the same set than as shown in Figure 5.4 (b), (d), and (f), respectively.

Increasing the applied voltage, the homogeneous mode becomes less dominant, and the spatial symmetry breaking is also seen in the non-subtracted data as in the case of the period

doubled structure displayed in Figure 5.5 (b) (compare with plate (d) in Figure 5.4). In the turbulent-like state the role of the homogeneous mode is even more reduced, and almost all dynamic features can be grasped from the non-subtracted data (cf. Figure 5.5 (c)). Moreover, in the ‘non-subtracted’ representation a clear process of nucleation and growth of high potential domains followed by a massive and abrupt annihilation is clearly seen (see red triangular objects in Figure 5.5 (c)).

5.4 CASE 2: CE/WE DISTANCE OF 5 mm

Results obtained with the second experimental configuration, i.e., case 2, in which the distance between the CE and the WE was reduced to 5 are shown in Figure 5.6. Again, three sets of the global current time series followed by the corresponding spatiotemporal evolution of the inhomogeneous part of the interfacial potential are shown. From (a) to (e) the applied voltage was increased. In the first case (plate (a), $U = 0.82$ V), the current oscillations are still relaxation-like as those shown in Figure 5.4 (a), but in contrast to them, they are more irregular and characterized by a longer phase during which the system is in a passive state. Accordingly, the spatiotemporal evolution of $U_{pp} - \langle U_{pp} \rangle_x$ shown in plate (b) exhibits some resemblance with the one shown in Figure 5.4 (b) in the sense that spatial structures arise mainly during the fast current transitions. Moreover, the spatial modulations can still be approximated by a sinusoidal structure with wave number 1, although the pattern is by far less regular. Furthermore, in contrast to above, the sign of the amplitude is identical on the current flanks with positive and with negative slopes.

Increasing the applied voltage, the average oscillation period becomes shorter. From the corresponding space-time plot shown in (d) it is apparent that an intermittent-like dynamics is present, i.e., short periods, in which structure pops up during the fast changes in current, as in Figure 5.6 (b), are interrupted by longer intervals during which the electrode is inhomogeneous during all phases of an oscillation of the global current. During these intermittent intervals the patterns resemble compact cluster-like structures. Moreover, these structures seem to rotate slowly around the electrode.

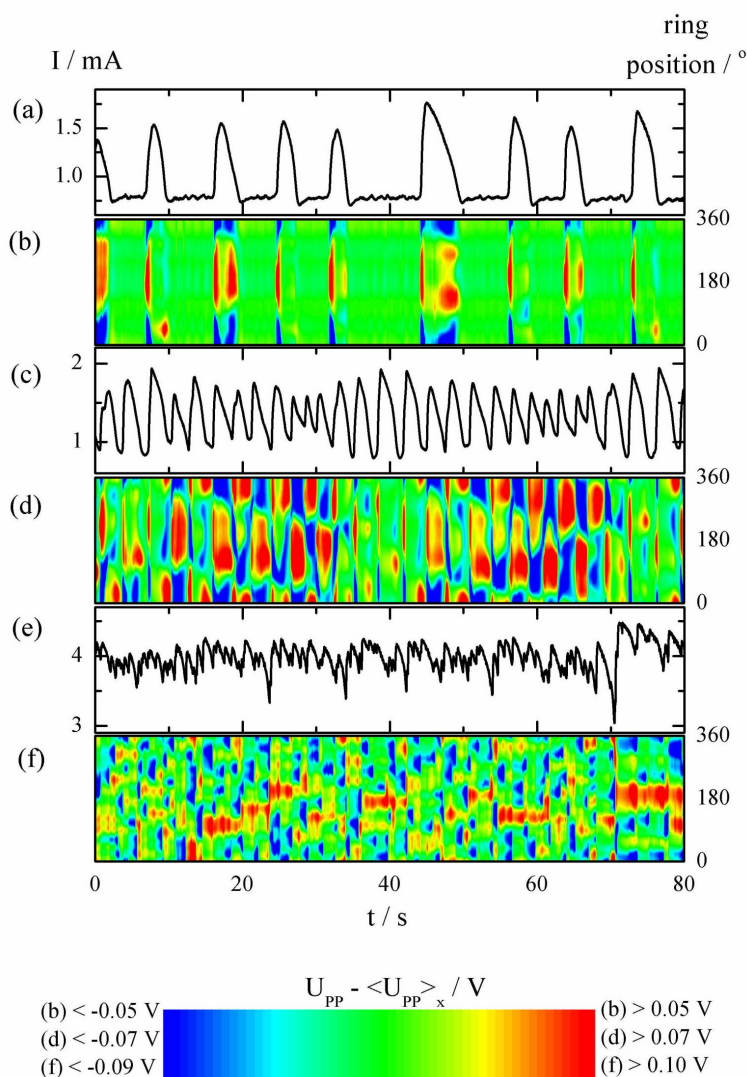


Figure 5.6: (a), (c), and (e): Current time series. (b), (d), and (f): The spatiotemporal evolution of the inhomogeneous part of the interfacial potential, $U_{PP} - \langle U_{PP} \rangle_x$, as a function of time and ring position. Applied potential U : (a) and (b) 0.82 V, (c) and (d) 0.89 V, and (e) and (f) 1.54 V. Data obtained with configuration ‘case 2’. The remaining experimental conditions are identical to those given in Figure 5.3.

A sudden transition from this state to more complicated motions is observed when increasing the applied voltage. Compared to the data depicted in Figure 5.4 (e), the current time series shown in Figure 5.6 (e) are clearly more irregular and the oscillation frequency is higher. The random nucleation of excited domains of high (red) interfacial potential discussed for the turbulent state of case 1 is also present here, as is seen in plate (f). However, as further discussed below, in this case these excited domains are smaller, and the turbulent state observed in Figure 5.6 (f) is indeed characterized by a higher number of excited modes when compared to the previous situation (Figure 5.4 (f)).

As done for the data of case *I*, for the three plots shown in Figure 5.6 the full spatiotemporal data, i.e., those containing the homogeneous mode, are displayed in Figure 5.7. In order to provide a more detailed visualization, only part of the sets shown in Figure 5.6 are displayed in Figure 5.7.

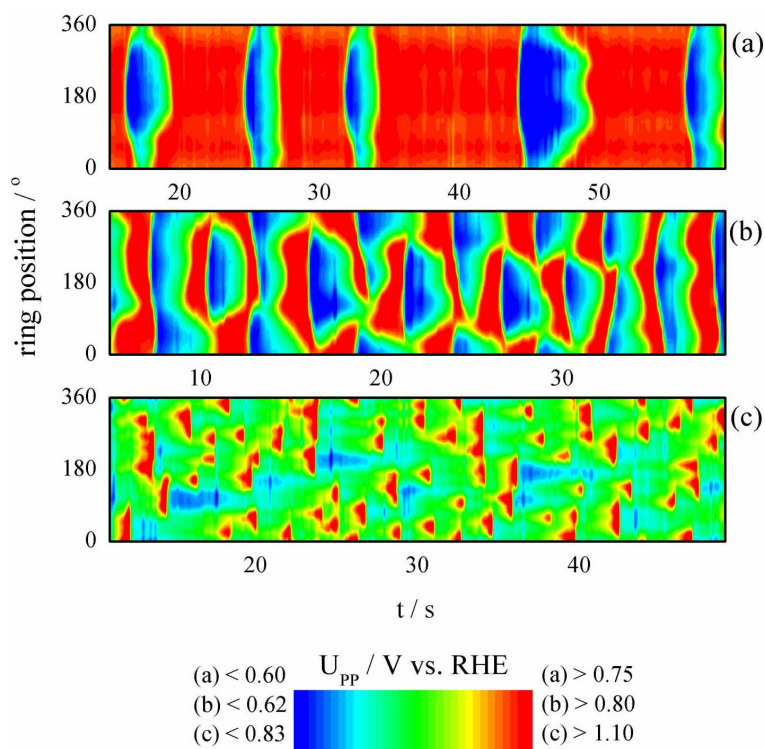


Figure 5.7: Spatiotemporal evolution of the interfacial potential, U_{PP} . Data shown in (a), (b), and (c) belong to the same set than that shown in Figure 5.7 (b), (d), and (f), respectively.

In contrast to case *I* (Figure 5.5), spatial structures are clearly noticeable even at low applied voltages, as can be seen in Figure 5.7 (a). The first appearance of the moving cluster-like domains illustrated in Figure 5.6 (d) are easily recognized in the U_{PP} picture in Figure 5.7 (d). Finally, the processes of nucleation/growth/annihilation of higher potential (red) objects characterizes the turbulent regime, but differently than in case *I*, the objects in Figure 5.8 (c) are smaller and more randomly distributed.

5.5 KARHUNEN-LOÈVE DECOMPOSITION

In this section the observed patterns just depicted are analyzed by means of Karhunen-Loève Decomposition (KLD), which was introduced in chapter 2. The particular goal here is to identify the spatially active coherent modes that govern the spatiotemporal patterns.

In order to do so, it seems convenient to start with the simplest observed patterns, namely the ones in the beginning of the oscillatory range at low U values. The results of the KLD of the data shown above in Figure 5.4 (b) at $U = 1.06$ V are displayed in Figure 5.8. In plate (a) the amplitude and shape of the first and second modes are shown, the eigenvalues and their cumulative contributions to the pattern are given in (b).

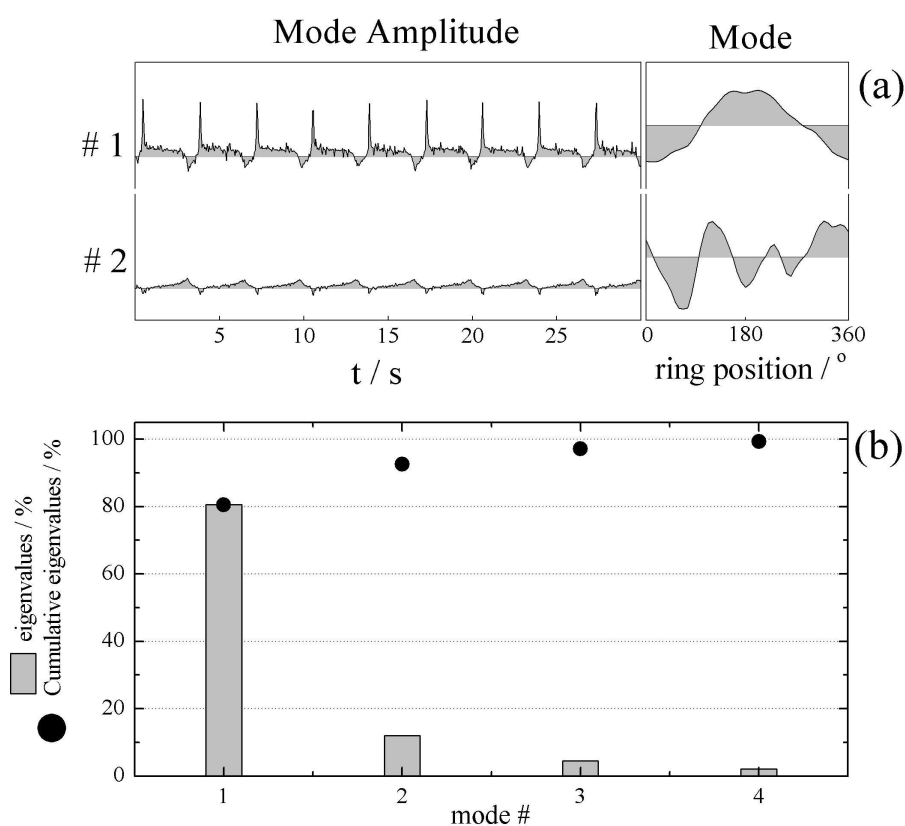


Figure 5.8: KLD of the spatiotemporal data given in Figure 5.4 (b). (a) Mode and mode amplitude, and (b) eigenvalues and their cumulative contributions as a function of the mode number.

The cumulative eigenvalues of the eigenmodes quantify how much of the observed pattern is captured when using these modes to reconstruct the dynamics. As is seen in Figure 5.8 (b), the first mode already carries nearly 80 % of the information contained in the original

inhomogeneous part of the pattern. When including the second and third modes, the cumulated energy amounts to 96.61 and 97.20 %, respectively.

The first mode resembles a Fourier mode with $n=1$. The fact already mentioned above that the spatial structure with wave number 1 is predominantly excited in one of the flanks of the current oscillation, can be seen in the corresponding amplitude time series. In contrast to the first mode, the second one does not resemble a Fourier mode. It corresponds to an additional spatial modulation of the sinusoidal structure.

Similar plots obtained from the data of case 2 (Figure 5.6 (b)) are shown in Figure 5.9.

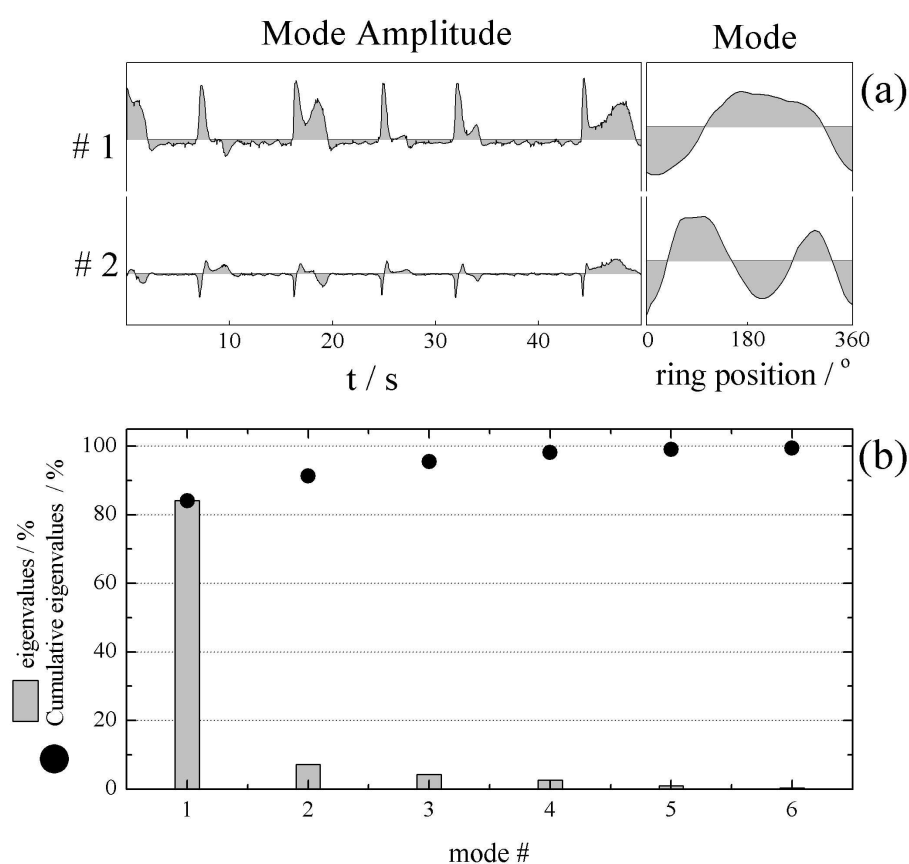


Figure 5.9: KLD of the spatiotemporal data given in Figure 5.6 (b). (a) Mode and mode amplitude, and (b) eigenvalues and their cumulative contributions as a function of the mode number.

The first mode in Figure 5.9 is still reminiscent of a sinusoidal mode. There are two main features of its time evolution: First, there are double peak structures which reflect that the pattern pops up with the same sign on the rising and falling part of the global current; second, the peaks in the time series of the first mode are broader than in case 1,

corresponding to a larger portion of an oscillation during which the electrode takes on an inhomogeneous state. In this case, the first mode is responsible for 84.5 % of the information contained in the original inhomogeneous data set. The cumulative energy corresponding to the first two and three modes is 91.36 and 94.98 %, respectively.

Space-time plots of the original inhomogeneous data and plots obtained by taking into account the first and the first two modes are depicted in Figure 5.12 for the two cases. In both cases, the dynamics is mainly captured by the first mode and when the two first modes are used, the reconstruction is already almost identical to the original pattern.

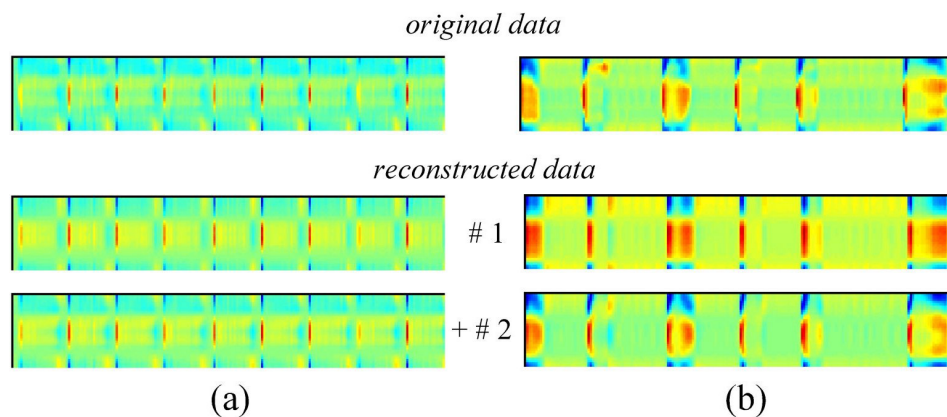


Figure 5.10: Original and reconstructed patterns with one and two modes for the data shown in (a) Figure 5.4 (b), and (b) Figure 5.6 (b).

As discussed above, the homogeneous mode has a dominant contribution at low U values, and Figure 5.11 illustrates this aspect. The KLD for case 1 is displayed in this figure. Here, the first mode corresponds to the homogeneous one and oscillates with the same shape as the observed global oscillations. Note that in this picture the amplitude scale of modes #2 and #3 is 5x the amplitude of the first mode. Moreover, the contribution of the homogeneous (first) mode to dynamics is about 99 %.

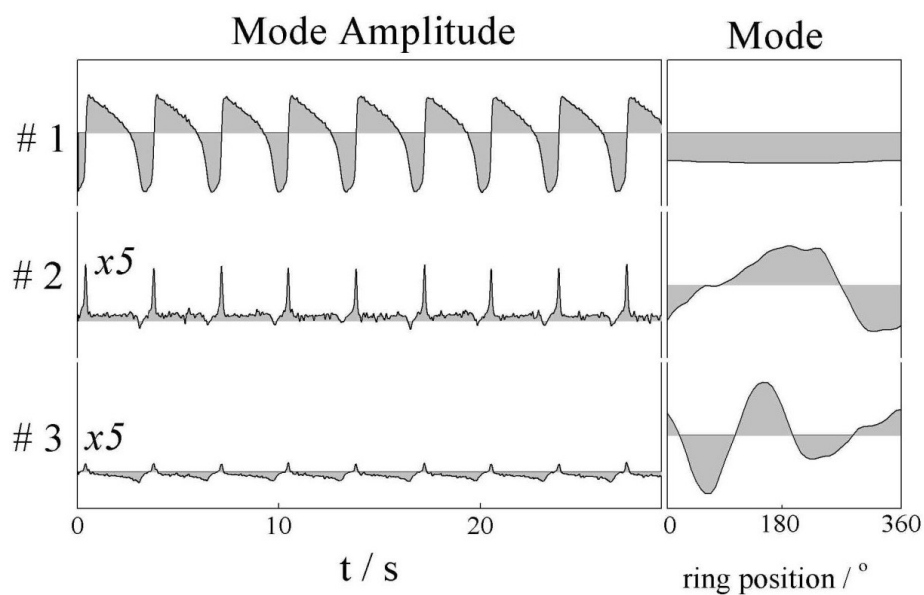


Figure 5.11: KLD of the spatiotemporal data given in Figure 5.7 (a) showing the mode and its amplitude.

Switching from the simplest patterns to the ‘most complicated’ ones, Figures 5.12 and 5.13 show the first eight modes with their respective amplitudes or ‘time series’ for the turbulent states depicted above in Figures 5.4 (f) and 5.6 (f), respectively.

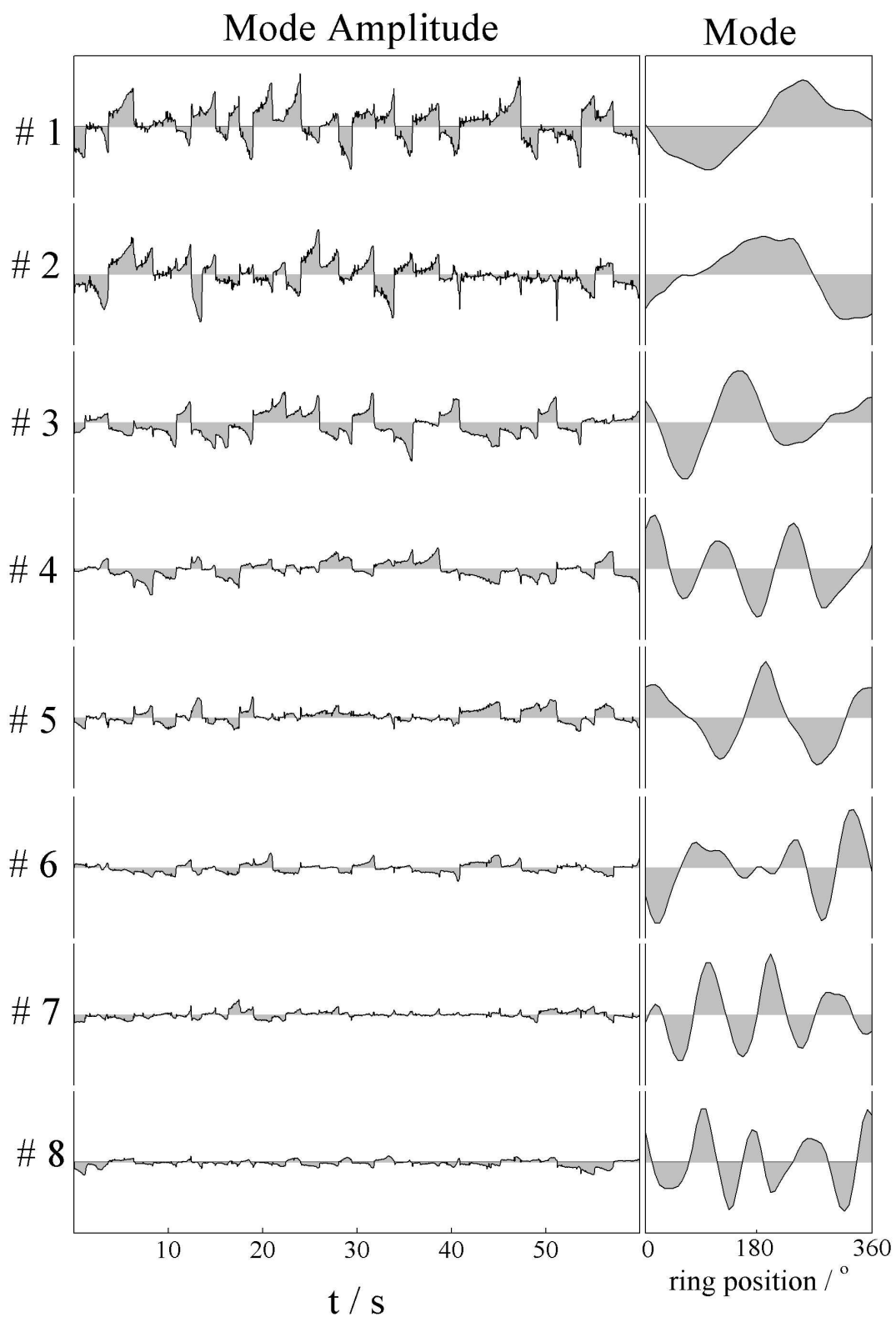


Figure 5.12: First eight modes and their amplitudes of the KLD for the spatiotemporal data shown in Figure 5.4 (f) (case I).

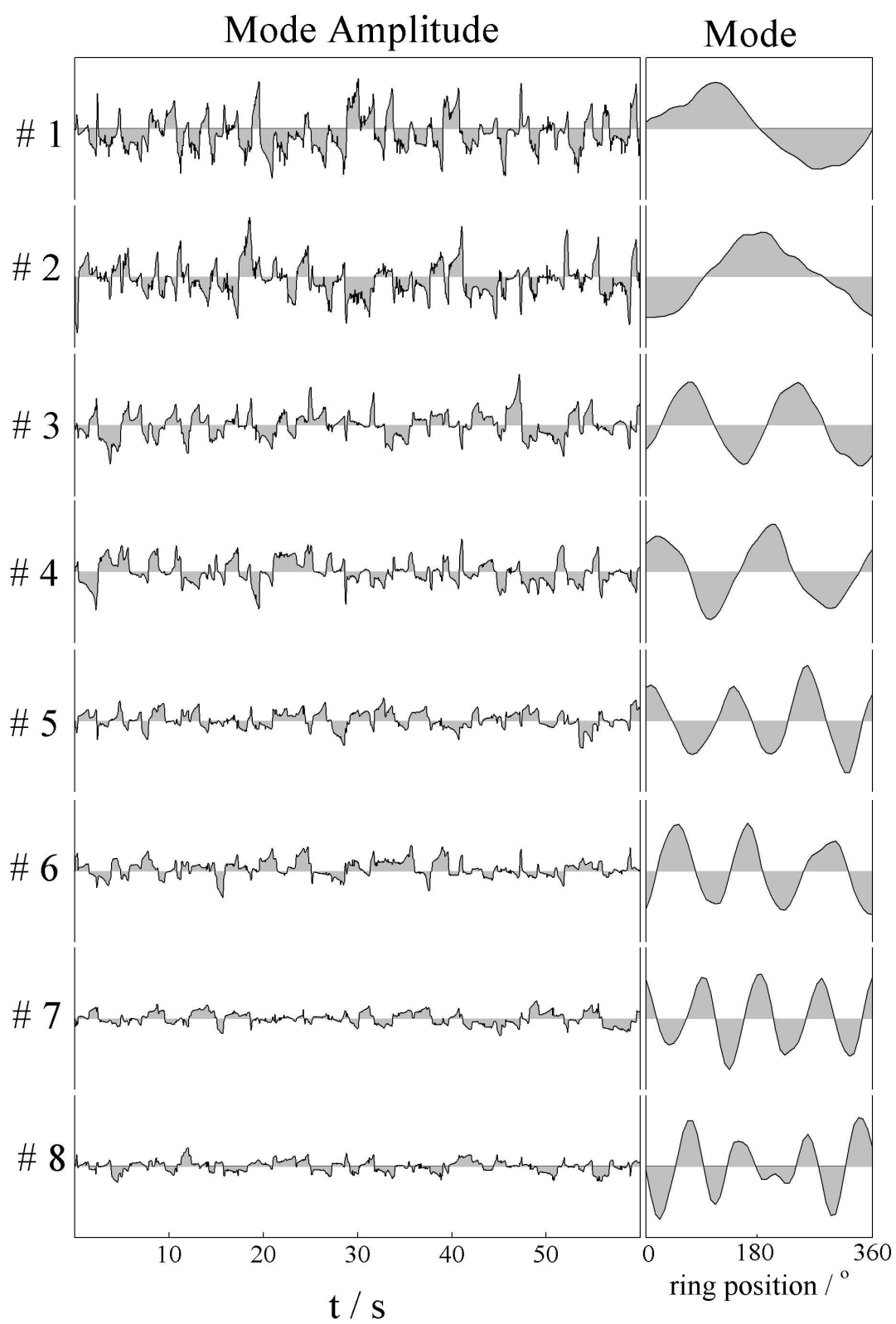


Figure 5.13: First eight modes and their amplitudes of the KLD for the spatiotemporal data shown in Figure 5.6 (f) (case 2).

In both cases the mode amplitudes are aperiodic, and the relative importance of higher modes is more pronounced in the case shown in Figure 5.13. With the exception of the first mode, the modes shown in Figure 5.12 are irregular and do not resemble Fourier modes. In contrast, the modes depicted in Figure 5.13 are more regular and, with exception of mode # 8, they could be approximated by sinusoidal structures. Moreover, modes with the same wave number appear in pairs and are shifted by about $\frac{1}{4}$ of the wavelength between each other, in such a way that the peaks of one mode (mode #2 in Figure 5.13, for instance) are always located at the position of the zero crossing point of their pairs (in the example, mode #1 in Figure 5.13). Hence, the phase relation is as the one of sines and cosines with the same wave number. This symmetry between the pairs of modes is easily seen when plotting each mode against its pair. For the case depicted in Figure 5.13 the curves look like almost perfect circles, the number of loops being equal to the wave number of the mode. In the other situation depicted in Figure 5.12, no symmetric circles are obtained.

The eigenvalues as well as their cumulative contributions corresponding to these two cases are depicted in Figure 5.14.

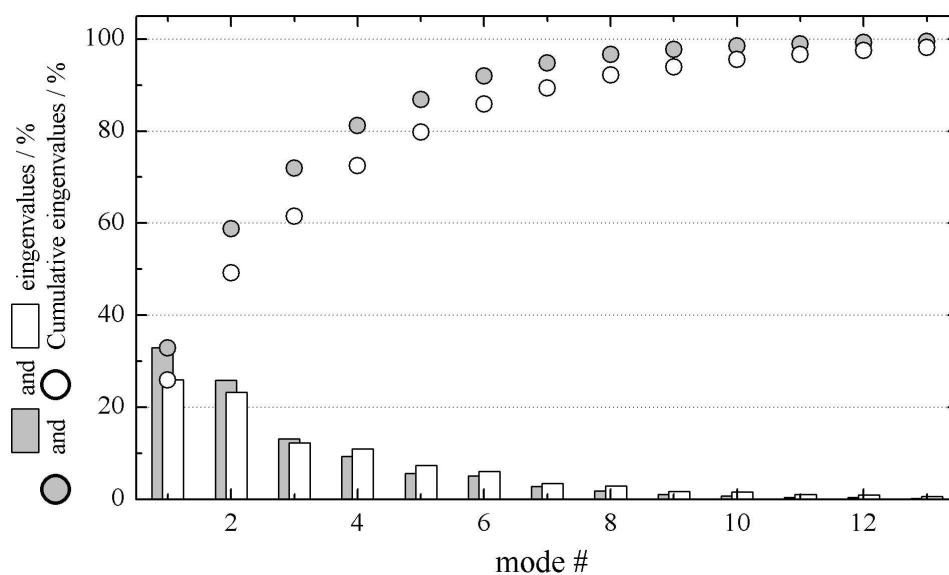


Figure 5.14: Eigenvalues and their cumulative contributions as a function of the mode number for the data shown in Figures 5.4 (f), case 1 (light gray) and 5.6 (f), case 2 (white).

The main conclusion to be drawn from Figure 5.14 is that in order to capture a certain amount of information contained in the original pattern, more modes are necessary in the case

of the smaller CE/WE separation. Considering, for instance, a level of cumulated energy in the order of 95 %, eight modes would be necessary in case 1, whereas two more modes would be necessary for case 2. Hence, the closer distance between the WE and the CE leads to more complex dynamics since more modes or dominant spatial structures are necessary to describe the dynamics than if the WE is further away from the CE.

The entire scenario involving the two experimental situations depicted above in Figures 5.4 and 5.6 including several other stationary experiments at intermediate voltages (not shown above) is summarized in Figure 5.15 in terms of the cumulative eigenvalues as a function of the number of modes at different applied voltages. Plate (a) refers to case 1 and plate (b) to case 2. In plate (c) the number of modes necessary to capture 95 % of the pattern is given as a function of the applied voltage.

As already discussed above, for low U values around 80 % of the spatiotemporal dynamics is captured by just one mode in both experimental configurations, and more modes are necessary when increasing U . In Figure 5.16 (a) it is apparent that there is a *continuous* decrease of the cumulative energy for a certain number of modes accompanying the increasing of U . In contrast, for case 2 shown in Figure 5.16 (b), a sharper decrease of the cumulative energy for a certain number of modes is observed. Indeed, as shown in Figure 5.16 (c), the number of modes necessary to capture 95 % of the spatiotemporal dynamics increases almost linearly with U in case 1 (full circles), whereas it shows a jump between 0.89 and 1.04 V and remains constant for higher U values for case 2 (open circles). This saturation value of ten modes shown in Figure 5.16 (c) for case 2 might reflect the experimental limitation of 50 points (or equivalently 7.2°) along the ring. Thus, since points between 7.2° are interpolated, smaller structures could not be seen in the present resolution.

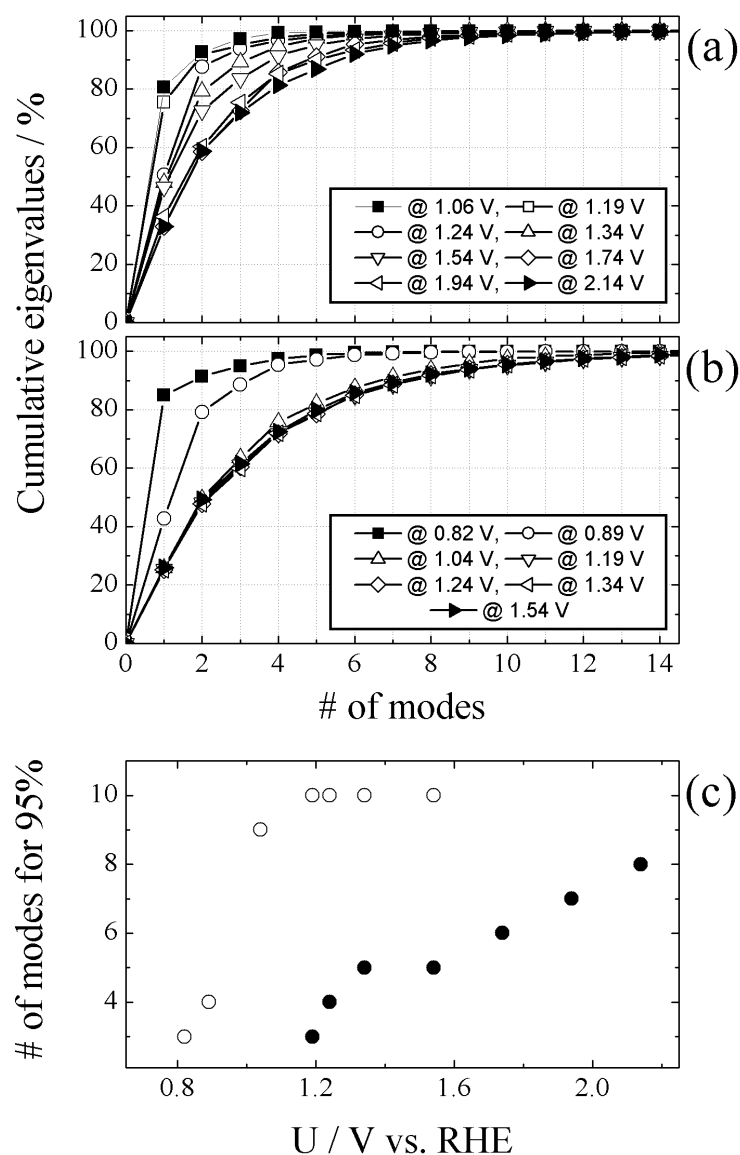


Figure 5.16: Cumulative eigenvalues as a function of the number of modes for different applied voltages. (a) case 1, and (b) case 2. (c) Number of modes necessary to capture 95 % of the pattern as a function of the applied potential. Full circles: case 1; open circles: case 2.

Figure 5.17 shows the sum of the first n eigenvalues as a function of the applied voltage. Neglecting the behavior of the first mode, the cumulative energy seems to vary continuously when increasing U in Figure 5.17 (a). In case 2, Figure 5.17 (b), the U region, in which the transition from simple to more complex motions takes place, is smaller and the transition occurs more abruptly.

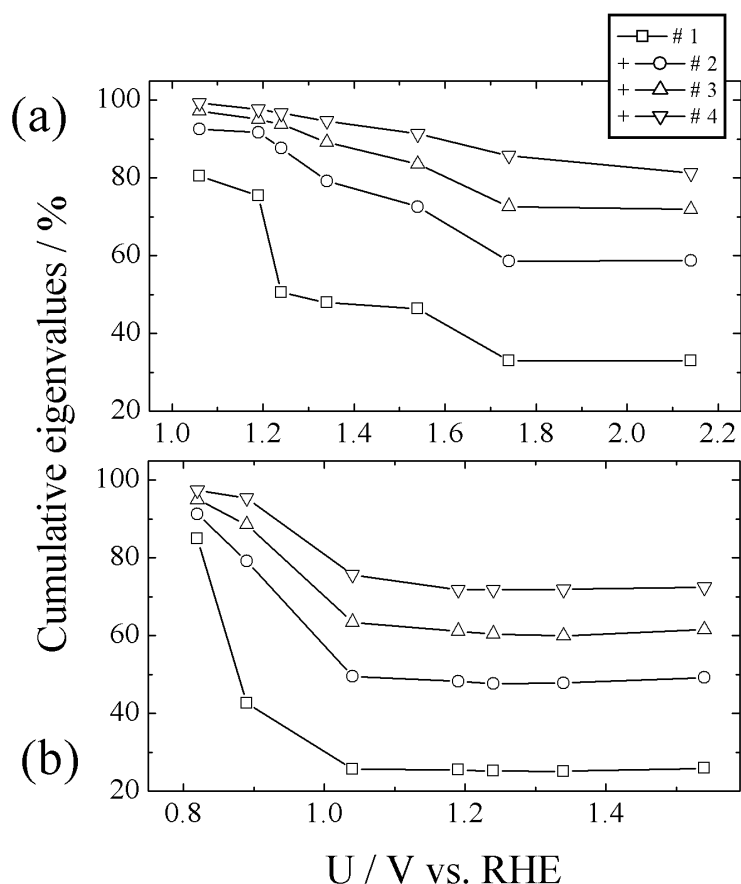


Figure 5.17: Cumulative eigenvalues of the first n modes with $n = 1, 2, 3, 4$ as a function of the applied voltage for (a) case 1, and (b) case 2. For mode number see symbols in the inserted chart.

5.6 DISCUSSION AND SUMMARY

Spatiotemporal patterns in the oscillatory $\text{Pt}|\text{H}_2\text{SO}_4, \text{Cl}^-, \text{Cu}^{2+}|\text{H}_2$ system when subjected only to the migration coupling were presented in this chapter. The two main results obtained are (a) a transition from a periodic state to a weakly turbulent state, and (b) the different complexity of the turbulent states for different distances between the CE and the WE.

The transition to turbulent states observed here is one of the rare examples (if not the first) of a transition to chemical turbulence in oscillatory media. Increasing the applied voltage, a laminar-laminar transition [56], in which the periodic pattern changes its form but the number of spatially excited modes remains small, is followed by a transition into a turbulent regime characterized by the excitation of several modes. The increase of the number

of excited modes with applied voltage was found accompanied by a decrease of the characteristic length scale of the pattern. This points to the fact that increasing U has the same effect as increasing the system size.

In chapter 2, the transition to turbulence in reaction-diffusion systems was discussed in the frame of the *complex Ginzburg-Landau equation* (CGLE). In this sense the transition to turbulent states was said to be associated to the so-called *Benjamin-Feir (BF) instability*. As pointed out by Christoph *et al.* [46, 78], since the mechanism underlying the appearance of the BF instability does not depend on the exact form of the coupling, this criterion can also be invoked to discuss transitions to spatially inhomogeneous oscillations in reaction-migration systems. The transition reported in this chapter is characterized by a decrease of weight of the dynamics of the homogeneous mode. It occurs from slightly modulated spatial structures to a turbulent regime.

An experimentally observed transition to chemical turbulence was reported in the chlorite-iodide-malonic acid (CIMA) reaction by Ouyang and Swinney [173]. Differently from the oscillatory dynamics reported here, they observed a transition from *stationary* Turing-like patterns to disordered states when changing the control parameter, namely the concentration of malonic acid. The authors referred to this finding as the first experimental observation of defect mediated turbulence in a reaction-diffusion system. Besides this ‘Turing turbulence’ [60], Ouyang and Flesselles [174] observed a transition from spirals to defect mediated turbulence in the Belousov-Zhabotinsky reaction. In this case, the control parameter was the sulfuric acid concentration, and convection instability was the main mechanism underlying the transition to turbulence. Examples of experimentally observed irregular patterns and chemical turbulence in heterogeneous catalyzed reactions are the reduction of NO with NH_3 on a Pt (100) surface [14] and the CO oxidation on Pt (110) [12, 175-178].

The second aspect to be pointed out consists of the effect of the distance between the CE and the WE. Considering cases 1 and 2, it was shown that the ‘more turbulent’ states are obtained for a closer CE/WE distance. This finding can be viewed as the first experimental proof of the theoretical prediction by Mazouz *et al.* [39] that the range of the migration coupling decreases with decreasing distance between the WE and the CE. Thus, when going from configuration ‘case 1’ to configuration ‘case 2’ the coupling range should become more localized. Hence, the smaller spatial correlation in the spatiotemporal patterns observed at

smaller CE/WE separation can be interpreted as being the result of the more localized coupling configuration 'case 2'. Moreover, this smaller correlation has been quantitatively inferred through KLD results which shows that more modes are required to capture the same amount of information of the original pattern in case 2 than in case 1.

There are some remaining, unanswered, questions. One relates to the search for universal dimensionless control parameter. One of which should quantify the distance from the thermodynamical equilibrium in electrochemical systems and depend on the applied voltage, the other one should describe the damping intrinsic in dissipative systems. This dimensionless control parameter would provide a more general understanding of the transition into chemical turbulence observed here. A second fundamental point not referred to so far is the role played by the chemistry in the present system, since turbulence has been observed only at lower copper concentration.